The evolution of restraining and releasing bend pairs: analogue modelling investigation and application to the Sea of Marmara

S. Bulkan[1], P. Henry[2], P. Vannucchi[1,3], F. Storti[4], C. Cavozzi[4], J. P Morgan[1,5].

[1] Royal Holloway, University of London, Earth Sciences Department, Egham, UK.

[2] CEREGE, CNRS-Aix Marseille Université, Marseille, France

[3] Dipartimento di Scienze della Terra, Universita' degli Studi di Firenze, Via La Pira, 4, Firenze, Italy

[4] NEXT – Natural and EXperimental Tectonics research group, Department of Chemistry, Life Sciences and Environmental Sustainability, University of Parma, Italy

[5] Department of Ocean Science and Engineering, SUSTech, Shenzhen, China

Corresponding author: Sibel Bulkan (Sibel.Bulkan.2015@live.rhul.ac.uk)

Key Points:

- Reproduces and explores, by analogue modelling, the effect of a releasing-restraining bend pair geometry for the western part of the NAF.
- Presents crustal strain patterns and associated topographic changes obtained from analogue model PIV Analysis.
- Experimental results are compared with the actual structural/topographic evolution of the Marmara Sea region.

Abstract

In spite of many specific studies focussing on the Sea of Marmara segment of the North Anatolian Fault (NAF), its deformation and stress accumulation pattern remain difficult to understand. In part this is due to the complexity of the transform fault system which here combines a releasing and restraining bend. In this study, we use analogue modelling to reproduce and monitor the strain patterns across a releasing and restraining bend pair. We also compare the strain evolution with the evolution of topographic changes.

The experiments reveal how the master right-lateral strike-slip fault system and newly formed fault zones change their geometry as displacement accumulates across a releasing and restraining bend pair. We find that the master shear zone develops from a single to a multi-branch fault system, with different branches active and dominant at different times. Comparison with the tectonic setting of the Sea of Marmara suggests that the western portion of the basin may be characterized by a fault shortcut associated with both a compressional regime and uplift of the Ganos Mountain.

1 Introduction

Continental transform faults can vary from single, pure strike-slip shear zones to complex domains with branching, bending or oversteps that partition and diffuse tectonic deformation (LePichon et al., 2001), while often creating adjacent releasing and restraining bends. In these complex systems current debate focuses on: i) the evolution of strain localization in different fault segments over time; ii) which fault segments tend to remain active over long periods of time; iii) to what extent fault localization controls the development of subsidence or uplift.

Here we use scaled sandbox analogue modelling to address the problem of how strain and surface relief develop during the evolution of a major fault system that contains adjacent restraining and releasing bends. We also apply this model to explore the potential evolution of the North Anatolian Fault (NAF) in the Sea of Marmara. In the simplified view taken here, we idealise the geometry of the Sea of Marmara as a releasing bend adjacent to the Ganos segment to the west, which is considered to be a restraining bend (Mann, 2007) (Fig. 1). We use a crustal master strike-slip fault system geometry derived from onshore and offshore tectonic maps (e.g. Armijo et al., 2002; Le Pichon et al., 2003; 2015; Becel et al., 2010; Grall et al., 2012, 2013).

Numerous studies have focused on the geology of the Sea of Marmara, the geometry of its basin-boundary faults from the Izmit to the Ganos segments (Fig. 1) (Armijo et al.,

1999, 2005; LePichon et al., 2001; Imren et al., 2001; Seeber et al.,2004, 2006; Okay et al., 2004; Carton et al., 2007; Laigle et al., 2008; Becel et al., 2010; Gasperini et al., 2011; Sorlien, et al.,2012; Kurt et al., 2013; Grall et al., 2012), and on slip rates over different time scales across different fault segments (Armijo et al., 2002; Flerit et al., 2003; Ergintav et al., 2009; Gasperini et al., 2011; Reilinger and McClusky, 2011; Grall et al., 2013; Akbayram et al., 2016; Hussain et al., 2016). Although faults in the Sea of Marmara have been thoroughly mapped, their overall tectonic setting is still controversial. Three model scenarios have been proposed (Fig. 2): 1) the pull-apart model (Armijo, et al., 1999, 2002), 2) the en-echelon fault segment model (Okay et al., 2000, 2004), and 3) the single throughgoing fault (LePichon et al., 2001, 2014; Sengor et al., 2014; Seeber et al., 2004, 2006, 2010; Kurt et al., 2013). A previous numerical model used to test these three scenarios found that a series of pull-apart basins along with a master strike-slip fault system could best reproduce the observed morphology of the region (Muller and Aydin, 2005; Hergert and Heidbach, 2011), including the reproduction of vertical structural offsets within the Sea of Marmara.

Previous scaled sandbox models have investigated the evolution of strike-slip fault systems in different kinematic environments, with and without crustal heterogeneities, with their main goal being to reproduce local pull-apart basin or pop-up geometries (McClay and Dooley, 1995; Dooley and McClay, 1997; Rahe el al., 1998; Sims et al., 1999; McClay and Bonora, 2001; Dooley et al., 2004; Wu et al., 2009; Dooley et al., 2012; Sugan et al., 2014), or specific evolutionary pathways (e.g. D'Adda et al., 2016). Analogue models have been used to study fault propagation and strain localization and accumulation (Adam et al., 2002; Adam et al., 2005; Dotare et al., 2016; Hatem et al., 2017).

The formation of strike-slip bends from stepovers and their topographic evolution has also been previously investigated with analogue models (Cooke et al., 2013; McClay and Bonora, 2001; Wu et al., 2009, Toeneboehn et al., 2018).

2 Methods

Here we combine scaled analogue modelling with Particle Image Velocimetry (PIV) analysis (Adam et al., 2005) to explore the geometry, topography, and shear strain patterns associated with the propagation and distribution of deformation along a major fault strand with adjacent releasing and restraining bends. A set of ten experiments was performed with varied model configurations. Here we present results from the most representative ones.

2.1 Model Setup

The experimental apparatus consisted of a sandbox with a 250 x 100 cm glass basal plate, equipped with two computer-controlled motors, and a "structured light scanner" to monitor the topographic surface of the model with a resolution of 0.71 mm in the x and y directions. Structured light scanning is also known as "point cloud" mapping. In structured light scanning a pattern, e.g. a regular grid of dots, is projected onto the surface to be scanned. The distortion of this grid is then used to determine surface relief. This provides an effective tool to comprehensively describe the vertical evolution of the model, i.e the uplift and subsidence of the system. It allows quantitative measurements to be easily made with relatively high precision (e.g. Nestola et al., 2013; D'Adda et al., 2016). Here we use an overhead NIKON-D5200 digital camera to record the model evolution at 6000x4000 pixel resolution. In this experimental setup, overhead camera captured images and structured light scanning provided elevation data for every 5 minutes of model deformation, i.e. for every 1.6 mm of displacement along the basal fault. Experiments were performed using a 1 mm-thick Plexiglas mobile plate that was cut to simulate a releasing-restraining band pair. This geometry approximates the geometry of the northern strand of the NAF at the Sea of Marmara (Fig 3). Dextral shear was imposed to the mobile plate by translating it at a constant displacement rate of 2 cm/h, with a total displacement of 5 cm in each experiment. The scale factor of the models was 1×10^{-6} (1cm ⇔ 10km), which models the 15 km-thick upper crust in the Marmara Sea region (Kende et al., 2017) as a 1.5 cm-thick sandpack. A grid with 1x1 cm squares was pressed on the surface of the sandpack to better monitor surface fault locations and the progression of surface displacement.

2.2 Materials

In the undeformed experimental multilayer, the brittle upper crust was simulated with a 1.5 cm-thick sandpack consisting of six 2 mm-thick alternating white and coloured quartz sand layers overlain by a 3 mm-thick white sand layer (Fig. 4). The density of the sieved sand was 1.670 g/cm^3 and the mean size of quartz grains was 224 μm (from Klinkmüller et al., 2016). The angle of internal friction was 33° with a peak cohesion of 102 Pa (e.g. D'Adda et al., 2016). To simulate the mechanical role of the viscous lower crust, a 2 mm-thick basal layer of PDMS XIAMETER silicone putty mixed with barite powder was placed at the base of the sandpack. The density of this layer was 1.15 g/cm^3 and its dynamic shear viscosity was

1.4 x 10^4 Pa-s (after Cappelletti et al., 2013). The mechanical and physical properties of the materials used in the experiments are shown in Table 1.

2.3 Particle Image Velocimetry (PIV)

Particle Image Velocimetry is an optical image correlation method that is often used to monitor displacement/velocity fields in laboratory flow and deformation systems. This technique is commonly used for dynamic flow analyses, heat transfer, and soil mechanics (White et al., 2001; Adam et al., 2002; Adam et al., 2005; Wolf et al., 2003), and has also been applied to structural geology modelling (Adam et al., 2005; Funiciello et al., 2006; Hatem et al., 2017). Here we use interrogation areas of pairs of images in 64x64 and 32x32 pixel subregions, and derive the best-fit particle displacement in the interrogation areas with the cross-correlation method implemented in the free MATLAB-based PIV-Lab Software package (Thielicke and Stamhuis, 2014). This lets us obtain velocity fields from incremental particle displacements throughout the experiments. PIV-Lab provides incremental displacement fields from 76 images. From these we calculate incremental shear rates and shear strains. In particular, we determine the velocity gradient matrix by measuring the derivatives of the u and v velocity components in the x and y directions, respectively, namely $\partial u/\partial x$, $\partial u/\partial y$; $\partial v/\partial x$, and $\partial v/\partial y$, with the velocity gradient matrix being used to compute incremental strain tensors. The incremental horizontal shear rate is approximated as the velocity gradient perpendicular to the velocity discontinuity applied at the base of the model ($\partial u/\partial y$).

Angular velocity is calculated from the curl of the velocity field, and shows the shear accommodated by faults in any orientation.

The incremental areal strain is the sum of the diagonal components of the strain tensor ($E_{xx} + E_{yy}$):

$$E_{xx} + E_{yy} = \partial u/\partial x + \partial v/\partial y \quad (1)$$

The incremental rate of topographic change is calculated by subtracting the measured topography at time *n-1* from the topography at time *n*, corrected for any displacement that occurred between times *n-1* and *n*. Specifically, we determine the material derivative of topography, i.e. the change in topography over a time-step that follows surface motions. To do this, we measure relief on the fine mesh of points available for each topographic measurement, and use an interpolation of the velocity field determined from the coarser mesh

of PIV sampling subregions to backtrack each sample point on the fine mesh to where it started at the end of the previous time step. The difference between these measurements is the change in relief felt by this surface point over the time step. Computed rates of incremental topographic changes are then related to the incremental strain patterns in order to understand how relief is generated. Shear rate maps show how much shear deformation takes place during each step of the model, while areal strain maps show the rates of extension and compression in each area. In general, areal strain maps display higher noise than shear strain maps. However, the resulting strain patterns correlate well with the results obtained from the topographic changes.

3 Experimental Results

3.1 Strain and Topographic Evolution

In early stages of deformation, as the basal plate is activated by dextral relative displacement, a principal shear zone develops that mimics the geometry of the underlying basal master fault (Fig. 5a). Incremental shear rate analysis shows that this initial principal shear zone is discontinuous, with a left-stepping offset coincident with the location of the restraining bend (Fig.7a). This offset also corresponds to a zone of topographic build up that is expressed as a pop-up structure. Uplift is fastest over the eastern half of the restraining bend, where strain patterns show that compression, indicated as negative areal strain, is localized along the edges of the topographic high, while its top experiences a little spreading as indicated by slightly positive areal strain (Figs. 7b, c). In contrast, subsidence above the releasing bend is accommodated by a major linear depression (Fig. 5b). The extension rate is higher along the releasing bend, which leads to subsidence and graben development (Fig.7c). A subsidiary fault zone parallel to the main graben splays from the eastern portion of the right-lateral strike-slip master fault system. This produces subsidence around the branching point and develops as a shallower basin. East of the releasing bend, the master fault system generates a narrow zone of shear localization without developing any striking topographic features (Fig. 7b).

Between the 25 mm and 30 mm of displacement, a new fault zone develops in the releasing bend, and branches out to the south of the principal shear zone. The incremental shear map allows us to observe how this new shear zone breaches the left-step that previously developed. Shear is partitioned between this new fault zone and the older fault system that more closely mimics the basal discontinuity (Fig. 7d). The new fault zone is located

197 southward of the previously developed pop-up structure, which leads to cessation of major
198 compression and de-activated of its eastern sector (Fig. 7e). In this western sector of the fault
199 system, alternating compression and extension occurs to the north of the basal master fault
200 system, while to the south, less intense opposite-alternating strain areas are present (Fig. 7f).
201 This strain pattern of compression and extension only partially corresponds to model uplift
202 and subsidence, with uplift being less prominent than in the earlier phase, but more
203 widespread, while subsidence occurs at the intersection of the releasing and restraining
204 bends, and along part of the latter. Within the releasing bend, subsidence is fastest around the
205 branching point of the new shear zone (Fig. 7e). Although some digital noise (a PIV
206 processing artefact) is present, figure 7f shows three domains of areal extension,
207 corresponding to the main graben, the eastern graben and the new fault zone.
208 With increasing displacement to between 45 mm and 50 mm of horizontal translation
209 of the mobile basal plate, the new southern fault accommodates most of the shear strain
210 deformation in that region of the model, and a strongly compartmentalized pull-apart basin
211 eventually develops (Fig. 5e). Development of a doubly-branched fault results in: a) the basin
212 becoming asymmetric, b) the depocenter becoming localized near the branching point, after
213 having migrated to the east, and c) subsidence propagating north, eastward of the releasing
214 bend (Figs. 7g-i). To the west, minor uplift characterises the region of the restraining bend,
215 with persistent alternating extensional and compressional areas.

216 ***3.2 Shear zone development and migration***

217 The maps of the angular velocity rate or vorticity (1/sec) show how fast the reference
218 points on the surface of the experiment are rotating (Fig. 6), with horizontal velocity vectors
219 also superimposed. In general, the vorticity patterns highlight regions of active strike-slip
220 deformation.
221 Shear rate and vorticity have very similar spatial patterns (compare Figs. 7a, 7c, 7e). The
222 major shear zone is characterized by dextral shear. A common feature in figure 6 is a
223 reduction in vorticity at the intersection between the releasing bend and the strike-slip fault
224 segment to the east.
225 Between the 15-20 mm displacement steps (Fig. 6a), vorticity is concentrated in the
226 western portion of the releasing bend where displacement vectors rotate clockwise. In the
227 restraining bend, clockwise rotation is present in an area of low vorticity (Fig. 6a).
228

Between 25-30 mm of overall displacement (Fig. 6b), the vorticity decreases in the releasing bend, as deformation is partitioned into a newly formed shear zone that intersects the releasing bend. In contrast vorticity increases at the restraining bend. Between 45-50 mm of overall displacement (Fig. 6c), the vorticity remains lower along the western part of the releasing bend. However, vorticity increases in the southern newly formed shear zone, while decreasing in the northern part of the releasing bend. The restraining bend also experiences decreasing vorticity. In this interval, the northern region moves SW toward the migrating shear zone.

4 Tectonic Setting of the Sea of Marmara

Before discussing the potential implications of the above modelling for the evolution of the Sea of Marmara region of the NAF, we briefly review its tectonic setting. The Sea of Marmara is a basin controlled by strike-slip tectonics (LePichon et al., 2014). Strike-slip deformation along the eastern part of the NAF has been constrained by several techniques. Geodetic measurements indicate ≈25 mm/yr of slip (Reilinger et al., 2006), while geologically-inferred motions are inferred to be ≈18 mm/yr in the last 10k years (Hubert-Ferrari et al., 2002; Kozacı et al., 2009), which suggests that some plate deformation is also being accommodated away from the main fault. Total slip on the eastern branch of the NAF has been estimated to be between 30-75 km (Barka and Gülen, 1989; Herece and Akay, 2003; Hubert-Ferrari et al., 2002; Şengör et al., 2005). In the west of Anatolia, plate motion is partitioned between the different NAF fault strands, with the NAF-N strand accommodating ~80% of total slip (Reilinger and McClusky, 2011). Geological estimates in general support this determination, with a minimum of 52±1 km cumulative dextral displacement in the Sea of Marmara region and additional ~15 km displacement across the Duzce fault (Akbayram et al., 2016). However, this displacement might record only post-Oligocene activity within the NAF (Sengor et al., 2005). West of the Sea of Marmara, displacement has been estimated to be between 40-80 km across the Ganos Fault (Armijo et al., 1999, Okay et al., 2004).

Slip rates on the order of 15-20 mm/yr have been inferred for different segments of the NAF-N (Kurt et al., 2013; Grall et al., 2013; Aksoy et al., 2010; Meghraoui et al., 2013). Most of these estimates imply that slip on the NAF-N at the eastern end of the Sea of Marmara is transferred to the Ganos Fault to the west of the basin and, ultimately, to the Aegean Sea (LePichon et al., 2014). However, data from the Gulf of Izmit imply much lower average slip rates: ~9 mm/yr over the past 10ky (Gasperini et al., 2011).

Measurements along the NAF-S are less abundant. These suggest 16-26 km of displacement (Koçyiğit, 1988; Özalp et al., 2013; Şengör et al., 2005), with slip rates of ≈4 mm/year over the past 10-15 ka. (Gasperini et al., 2011).

The Sea of Marmara is characterised by three tectonic depressions: the Çınarcık, Central, and Tekirdağ basins (Fig. 1). They are controlled by active fault zones, which link up in the so-called Main Marmara Fault (MMF) (Okay et. al., 2000; Le Pichon, 2001). These basins are separated by two NE-trending transpressional ridges, the Western High and the Central High, where the seafloor shallows to 570 and 380 m below sea level, respectively (Fig. 1). The position and migration through time of the depocenters appears to be related to the evolution of a releasing bend and to slip along the MMF (Grall et al. 2012). In the Çınarcık and in the Central Basins the active fault is located toward the north of the basins, while in the Tekirdag basin deformation is active in the south (Armijo et al., 1999; LePichon et al., 2001, 2014; Okay et al. 2004; Carton et al., 2007; Grall et al. 2012; Kurt et al., 2013). However, some ambiguity still persists. For example, there are uncertainties regarding the kinematic importance of a fault system that intersect the Çınarcık Basin in the central part and join the Izmit fault (Carton et al., 2007; Grall et al., 2012). To the south of this fault system in the Çınarcık Basin, Becel et al. (2010) observed low angle normal faults connecting to a south transtensional zone that seems to have accommodated early Pliocene stretching.

The Çınarcık Basin reaches a depth of 1270 m and contains 4-6 km of sediments (Carton et al., 2007). The Central Basin is 1250 m deep, with up to 6 km of syn-kinematic sediments, and the Tekirdağ Basin is 1130 m deep with >3 km of sediments (Bayrakci et al., 2013; Kende et al., 2017). Due to the lack of direct sampling, age-estimates for these sub-basins are inferred from models built from geophysical imaging of their geometry, estimates of the rates of sediment supply, and thermal modeling (Seeber et al., 2004, 2006; Carton et al., 2007; Sorlien et al., 2012; Grall et al., 2012; Kurt et al., 2013). Seismic imaging in deep basins has been proven successful, as evident in the deep Marmara Sea. The main active faults within the sedimentary basin of Marmara Sea have been seismically imaged, in depths down to 6 km below the sea floor (Becel et al., 2010). According to age estimates, the onset of basin formation occurred between 5 to 3.5 Ma in the southern part of the Sea of Marmara, in an area encompassing all the three deep sub-basins and also the Imrali basin (Sorlien et al., 2012, Grall et al., 2012). Starting at about 2.5-1.5 Ma, subsidence accelerated along the currently active master fault system and progressively migrated towards the west, in the

Tekirdağ basin, and towards the east in the Çınarcık Basin. The Tekirdağ basin's growth was associated with 25-30 km of strike-slip displacement on the master fault system, located in the southern edge; this occurred over the past 1.4 to 1 Ma (Seeber et al., 2004; Okay et al., 2004; LePichon, 2014). In the Tekirdağ basin, subsidence has migrated to the west and sediments are thicker in the east (Seeber et al., 2004). The Çınarcık Basin, with the master fault system located at its north, started to grow from the west around 2.5-1.5 Ma. Later on, the depocenter migrated to an intermediate area at about 1.4 Ma and, eventually, to its present location at about 1 Ma (Carton, 2007; Sorlien et al., 2012; Kurt, 2013).

The Sea of Marmara terminates westward against the Ganos Mountain. This is a region of about 1000 m of elevation around the junction between the Ganos bend and the MMF (Fig. 1). Ganos Mountain lies north of and trends parallel to the Ganos fault for about 35 km, with an almost uniform width of 8-11 km. Geological evidence indicates that the northern slope of the Tekirdağ basin represents the direct submarine continuation of the Ganos Mountain's southern slope, which implies there has been about 1100m of subsidence of the eastern flank of the mountain (Okay et al., 2004). Subsidence and uplift seem to be controlled by the Ganos bend, working as a buttress that concentrates compression (Seeber et al., 2004). Armijo et al. (1999) interpret the Ganos mountain uplift to be related to early Pliocene compression that was responsible for fold growth and then deactivated at ≈5 Ma by the Ganos Fault, which offsets these folds of about 80 km. Okay et al. (1999), instead, consider the uplift to be still active and linked to thrusting on a limb of a negative flower structure.

5 Discussion

5.1 Experimental limitations

Before analysing differences and similarities between models and nature, some major experimental limitations need to be pointed out. First of all, a typical limiting factor in sandbox modelling is the lack of fluids to permeate the experimental crust, both in host rock pores and localized within shear zones. Pore fluid pressure is undoubtedly a major factor that can shape deformation patterns and fault activity in nature (e.g. Chester et al., 1993). Other significant oversimplifications in the sandbox experiments are their lack of a geothermal gradient, lack of mineral reactions constraining rock rheology variations, and lack of an isostatic and flexural response to tectonic deformation. A specific feature of most experiments that simulate strike-slip faulting is the localization of the master shear zone by a

sharp boundary between nondeformable, mobile basal plates. This is not anticipated to be the most appropriate analogue to shear localization in nature at the scale of the entire crust (e.g. Schreurs, 2003). In our model, we used a 2 mm-thick silicone layer, scaled to the relative thickness of the viscous lower crust in the study of Kende et al. (2017), to better approximate the natural situation. Differences in the viscosity or thickness of this layer will shape how efficiently basal displacements are transferred to the shallower crust.

Additional oversimplifications affect these model results. The experimental crust is assumed to be mechanically homogeneous, without any heterogeneity or inheritance that might influence the deformation pattern. For example, heterogeneities in the crust deformed by the NAF system have been proposed to play an important role in strain localization (LePichon et al., 2014). Moreover, the shape of the master strike-slip right-lateral fault system in the experiments is simplified with respect to nature (Fig. 7). Since the purpose of our experiments is to obtain insights on the role of the strike-slip fault geometry in controlling subsidence and uplift patterns in adjacent regions, we do not attempt to reproduce all details of the tectonic pattern of the Marmara Sea. In spite of its limitations, analogue modelling has been widely proved to provide a useful tool for investigating tectonic processes (e.g. Koyi, 1997; Schreurs et al., 2006, 2016; Corti, 2012; Dooley and Schreurs, 2012; Gravelau et al., 2012).

5.2 Correction for Earth sphericity

To better compare analogue modelling results with the major tectonic features associated with the Sea of Marmara fault system, it is helpful to correct the “flat geometry” of model experiments for Earth sphericity and the overall small-circle geometry of the plate boundary fault system (Fig. 8). For this purpose, we use a Hotine-Oblique Mercator projection along the pole of rotation that represents the relative motion between blocks on either sides of the transform fault (e.g. Le Pichon et al., 2003). Unlike the WGS84 projection, the Hotine-Oblique Mercator projection customizes the map for a particular location and linear unit of measure (Engels and Grafarend, 1994). The rotation poles assumed for the Anatolia/Eurasian rigid plate motion and between Eurasia and a hypothetical "Marmara block" located between the northern and southern NAF branches are given in Reilinger et al., (2006).

5.3 Strike-slip fault system evolution and strain localization in the model and in the natural case

The experimental deformation pattern produced by a fault geometry with adjacent releasing and restraining bends shows the development of an asymmetric pull-apart basin with associated development of sub-basins and relative topographic highs. The pull-apart basin morphology is caused by increasing offset along the master strike-slip fault system. This simple geometric model can reproduce the first-order morphology of the Marmara Sea, without need for other external factors such as extension linked to the Aegean Sea. This finding is in line with the results of numerical models tested by Muller and Aydin (2005). However, our model is more effective at capturing the potential evolution of this fault system, since it has the capacity for new faults to form with progressive deformation, and can also model the topographic responses to these changes. In our model, for example, the fault system's evolution includes the progressive smoothing of the restraining bend buttress, accompanied by a transition from a single to a multi-branch fault system, with different branches active and dominant at different times. Overall, subsidence in basins is driven by the activation of different dominant strike-slip fault zones that locally generate extension and compression. Although these characteristics of these model experiments also typify tectonic features described for the Sea of Marmara, specific similarities and differences are present. Model experiments develop an asymmetry of faulting that is generally more localised in the fixed northern part of the model. In the Sea of Marmara, however, most NAF branching occurs at the expense of the Anatolian block, different than the observed model behaviour, in particular in its initial phases. This difference in fault branching may arise from the (known) heterogeneous crustal thickness observed in the Eurasian and Anatolian plates adjacent to the Sea of Marmara (Kende et al., 2017), while our models start with a homogeneous crustal thickness. We will see that predicted and observed surface relief are more consistent between model and nature.

Starting from the east, the releasing bend in the model is controlled by a shear zone that maintains a quasi-steady state position throughout the experimental evolution, while concentrated subsidence to the north or to the south of the shear zone creates major asymmetries in the basins. In the Çınarcık Basin and Central Basin, strain seems to have migrated northward and localized near the northern edge of a broader deformation zone (Armijo et al., 2002; Le Pichon et al., 2014, 2016; Kende et al., 2017; Sengor et al., 2005, 2014). There, the MMF has been nearly at steady state for at least 400 kyrs (e.g. Sorlein et

al., 2012; Grall et al., 2012). In spite of this difference, the model successfully reproduces both the modern boundary fault location on the northern side of the basin, and the asymmetric shape of the Cinarcik Basin with its steep northern slope and a gentler slope in the south (Fig. 8c). In fact, geological, seismological and geodetic evidence all indicate that the main active fault in the Cinarcik Basin is currently the Prince Island fault along the northern edge of this basin (Seeber et al., 2006; Bohnhoff et al., 2013; Ergintav et al., 2014), and also indicate that sediment thickness has increased towards the north (Seeber et al., 2006; Kurt et al., 2013; Grall et al. 2012; Le Pichon et al., 2014, 2016; Kende et al., 2017). The model also is consistent with the reduction in slip rates – from 15-20 to 9 mm/yr – in the Gulf of Izmit, as a persistent ≈50% reduction in vorticity is associated with the intersection of the releasing bend and the strike-slip segment to the east (Fig. 6).

In the western region of the model, the master shear zone migrated to the south by development of a "short-cut fault". Westward of the Sea of Marmara, localization of strain to the south seems to occur in the region of the Western High and Tekirdag Basin (Okay et al. 1999; Seeber et al., 2004; Şengör et al. 2014; Henry et al., 2018). According to Seeber et al. (2004), the Tekirdag Basin is controlled by the interaction of the restraining bend and the master transform fault at depth. The result is oblique slip on a non-vertical master fault which has caused the migration of shear from north to south. In our experiment, instead, the concentration of shear to the south is related to the development of a new fault zone that cuts across the restraining bend. This deformation style is not clearly visible in the Sea of Marmara. However, the kinematic importance of the Central Fault System in the Central Basin is at the moment poorly constrained. The Central Fault System and the MMF have been described as two distinct fault systems, but uncertainty exists regarding the relative roles of these two fault systems (LePichon et al., 2015), which could in fact be more interconnected than previously supposed. Another difference between the experiments and the Sea of Marmara is that the experiments have an asymmetry of faulting that generally seems opposite to that observed in nature. The experiments generate fault systems that splay towards the fixed 'northern' plate of the experiment. In contrast, in the Sea of Marmara, most NAF branching takes place within the southern Anatolian block. This difference may be a consequence of heterogeneous crustal thicknesses within the northern Eurasian and southern Anatolian Plates [Kende et al., 2017], while in our model each plate has a constant crustal layer thickness. In the following section, we will see that the topographic evolution is more consistent between experiments and nature.

5.4 Subsidence and uplift patterns in the model and in the natural case

The topographic evolution of the model shows that subsidence progressively concentrates towards the east, in a position that would correspond to the Çınarcık Basin. In the experiment, this corresponds to the longest-living portion of the initial graben, while further west the growth of a short-cut fault has transferred subsidence to the southward region of the strike-slip tectonic system. According to multichannel seismic, tomography, and heat flow data, the basement depth of the Çınarcık Basin reaches a maximum of >6 km, comparable to what occurs in the Central Basin and in the eastern part of the Tekirdag Basin. Sediment thickness maps for the Çınarcık Basin also imply that the main depocenter has gradually migrated eastwards over time (Carton et al., 2007). This may also be a consequence of slip obliquity at a fault bend (Seeber et al., 2004). Failure of the model to reproduce the eastward migration of subsidence that appears to have occurred in nature may indicate that this feature does not directly relate to the geometry of the master strike-slip shear zone, but to other factors, e.g. that there is asymmetric lower crustal flow underneath the extending region. In addition, the Cinarcik basin depocentre moved with the Anatolian plate but was fixed relative to the opposing Eurasian plate. This may have generated its characteristic shingled, asymmetric wedge of syn-kinematic strata (Seeber et al., 2010). In the western region of the model, the transition from one to two active fault branches caused the formation of an asymmetric basin similar to the present setting of the Tekirdag Basin.

Experimental topographic evolution shows that uplift in the restraining bend is more prominent when the southern fault zone has yet to fully form (Fig. 7b). This uplifted area correlates with the location of Ganos Mountain, which is indeed located to the north of the NAF. In the model, activation of the southern fault branch leads to a partial bypass of the restraining bend, and induces uplift to be replaced by subsidence in the eastern part of the previously formed pop-up. After this transition, uplift continues at a lower rate and progressively migrates westward. Geological and morphological observations of Armijo et al., (2002) show that in the Ganos Mountain uplift has stopped. Okay et al. (2004) propose that uplift in the Ganos area started at about 2 Ma. In the last few hundred thousand years the eastern end of the Ganos Mountain has collapsed by >1100 m. Seeber et al. (2004) proposed there has been progressive westward migration of subsidence in the area where the Ganos Fault crosses the shelf of the western Tekirdag Basin, while uplift has continued in the western part of the mountains throughout the Quaternary (Yaltirak, 2002). Moreover, tectonic inactivity of the fault bounding the northern side of Tekirdag Basin (Grall et al., 2018) may

be understood if the main active fault, which follows the southern side of the Basin, is considered to be a partial short-cut of adjacent releasing and restraining bends.

6. Conclusions

Our experimental results suggest that a strike-slip system with a releasing-restraining bend geometry does not favour the persistence of a single thoroughgoing fault system at shallow crustal levels. Instead it should evolve into a multi-branch fault system, with different branches active and dominant at different times. Comparing the model evolution with the geological record in the northern strand of the NAF within the Marmara Sea provides insights that help us to better understand the natural system.

I. In the eastern region of the analogue model, location of the main active fault zone northward of the main subsiding domain appears to simulate the development of the Prince Island Fault, i.e. the northern boundary fault of the Çınarcık basin and Central high. Both the analogue and the Çınarcık basins develop an asymmetric shape, with a shared steep northern slope and a gentler slope to the south.

II. In the western region of the Marmara Sea as well as in the analogue model, strain localizes to the south of the deformation zone/major fault. In the model, a major short-cut fault cuts through the restraining bend. This may also be the case in the Marmara Sea, although definitive evidence is lacking and the formation of the Western High and Tekirdag Basin may instead be controlled by the interaction of the restraining bend with the master transform fault at depth (Seeber et al., 2004).

III. Locations of the tectonic depressions developed in the model correspond with those of sub-basins in the Sea of Marmara. In particular, in the model the principal depocenter is located in the eastern part, similar to what happens in nature regarding the location of the currently active depocenter in the Çınarcık Basin.

IV. In the model, uplift associated with the restraining bend is located north of the major fault system and occurs early, when the southern fault zone is yet to be active. This evolution correlates extremely well with the occurrence of Ganos Mountain, which is indeed located to the north of the NAF. In the model, uplift ceases and migrates to the west when the southern fault zone forms. In nature, the main Marmara Fault can be interpreted as an incomplete short-cut that still allows for some compression and uplift of Ganos Mountain, although this short-cut was apparently successful in

deactivating the presumed fault scarp along the edge of the northern shelf in the Western Sea of Marmara.

Acknowledgments. This work was fostered by visits funded by the FLOWS-COST Action ES1301 "FLOWS". Analogue models were produced in the Analogue Modelling Laboratory "E. Costa" of the Department of Chemistry, Life Sciences and Environmental Sustainability, University of Parma, Italy. The paper benefitted by conversations with I. Watkinson and N. Scarselli at RHUL.

The MATLAB code for geological models is available on the Zenodo, open-access repository web-site (https://doi.org/10.5281/zenodo.3597335). All other sources used to build to geological models are published and referenced in the manuscript. Input files necessary to reproduce the model are available from the authors upon request (Sibel.Bulkan.2015@live.rhul.ac.uk).

References

Adam, J., Lohrmann, J., Hoth, S., Kukowski, N., & Oncken, O. (2002). Strain variation and partitioning in thrust wedges: High-resolution data from scaled sandbox experiments by 2D–3D PIV analysis. *Bollettino di Geofisica teorica ed applicata, 42,* 123-125.

Adam, J., Urai, J. L., Wieneke, B., Oncken, O., Pfeiffer, K., Kukowski, N., & Schmatz, J. (2005). Shear localisation and strain distribution during tectonic faulting—New insights from granular-flow experiments and high-resolution optical image correlation techniques. *Journal of Structural Geology, 27(2),* 283-301.

Adam, J., Klinkmüller, M., Schreurs, G., & Wienecke, B. (2013). Quantitative 3D strain analysis in analogue experiments: Integration of X-ray computed tomography and digital volume correlation techniques. *Journal of structural geology, 55,* 127-149

Akbayram, K., Sorlien, C. C., & Okay, A. I. (2016). Evidence for a minimum 52±1 km of total offset along the northern branch of the North Anatolian Fault in northwest Turkey. *Tectonophysics, 668,* 35-41.

Aksoy, M. E., Meghraoui, M., Vallée, M., & Çakır, Z. (2010). Rupture characteristics of the AD 1912 Mürefte (Ganos) earthquake segment of the North Anatolian fault (western Turkey). *Geology, 38(11),* 991-994.

Armijo, R., B. Meyer, A. Hubert, and A. Barka, 1999. Westward propagation of the North Anatolian fault into the northern Aegean: Timing and kinematics, *Geology, 27,* 267–270.

Armijo, R., Meyer, B., Navarro, S., King, G., & Barka, A. 2002. Asymmetric slip partitioning in the Sea of Marmara pull apart: A clue to propogation processes of the North Anatolian Fault. *Terra Nova, 14,* 80–86. 10.1046/j.1365-3121.2002.00397.x

Armijo, R., et al., 2005. Submarine fault scarps in the Sea of Marmara pull-apart (North Anatolian Fault): implications for seismic hazard in Istanbul, *Geochem. Geophys. Geosyst, 6,* Q06009, doi:10.1029/2004GC000896.

Barka, A. A., & Gülen, L. (1989). Complex evolution of the Erzincan Basin (eastern Turkey). *Journal of Structural Geology, 11*(3), 275-283.

Bayrakci, G., Laigle, M., Bécel, A., Hirn, A., Taymaz, T., Yolsal-Çevikbilen, S., & Team, S. (2013). 3-D sediment-basement tomography of the Northern Marmara trough by a dense OBS network at the nodes of a grid of controlled source profiles along the North Anatolian fault. *Geophysical Journal International, 194*(3), 1335-1357.

Bécel, A., Laigle, M., De Voogd, B., Hirn, A., Taymaz, T., Yolsal-Cevikbilen, S., & Shimamura, H. (2010). North Marmara Trough architecture of basin infill, basement and faults, from PSDM reflection and OBS refraction seismics. *Tectonophysics, 490*(1-2), 1-14.

Bohnhoff, M., Bulut, F., Dresen, G., Malin, P. E., Eken, T., & Aktar, M. (2013). An earthquake gap south of Istanbul. *Nature communications, 4,* 1999.

Cappelletti, A., Tsikalas, F., Nestola, Y., Cavozzi, C., Argnani, A., Meda, M., & Salvi, F. (2013). Impact of lithospheric heterogeneities on continental rifting evolution: constraints from analogue modelling on South Atlantic margins. *Tectonophysics, 608, 30-50.*

Carton, H., Singh, S. C., Hirn, A., Bazin, S., De Voogd, B., Vigner, A., ... & Sevilgen, V. (2007). Seismic imaging of the three-dimensional architecture of the Çınarcık basin along the North Anatolian fault. *Journal of Geophysical Research: Solid Earth, 112*(B6).

Chester, F. M., Evans, J. P., and Biegel, R. L. (1993), Internal structure and weakening mechanisms of the San Andreas Fault, *J. Geophys. Res., 98*(B1), 771– 786, doi:10.1029/92JB01866.

Corti, G. (2012). Evolution and characteristics of continental rifting: Analog modeling-inspired view and comparison with examples from the East African Rift System. *Tectonophysics, 522,* 1-33.

Cooke, M. L., Schottenfeld, M. T., & Buchanan, S. W. (2013). Evolution of fault efficiency at restraining bends within wet kaolin analog experiments. *Journal of Structural Geology, 51,* 180-192.

D'ADDA P., LONGONI R., MAGISTRONI C., MEDA M., RIGHETTI F., CAVOZZI C., NESTOLA Y. & STORTI F. (2016) – Extensional reactivation of a deep transpressional architecture: insights from sandbox analogue modeling applied to the Val d'Agri basin (Southern Apennines, Italy). *Interpretation, 5,* 55-66.

Dooley, T., Monastero, F., Hall, B., McClay, K., & Whitehouse, P. (2004). Scaled sandbox modeling of transtensional pull-apart basins: Applications to the Coso geothermal system. *Geothermal Research Council Transactions, 28,* 637-641.

Dooley, T., McClay, K., Analog modeling of pull-apart Basins, (1997*) AAPG Bulletin, 81 (11*), pp. 1804-1826.

Dooley, T. P., & Schreurs, G. (2012). Analogue modelling of intraplate strike-slip tectonics: A review and new experimental results. *Tectonophysics, 574,* 1-71.

Dotare, T., Yamada, Y., Adam, J., Hori, T., & Sakaguchi, H. (2016). Initiation of a thrust fault revealed by analog experiments. *Tectonophysics, 684,* 148-156.

Hatem, A. E., Cooke, M. L., & Toeneboehn, K. (2017). Strain localization and evolving kinematic efficiency of initiating strike-slip faults within wet kaolin experiments. *Journal of Structural Geology, 101,* 96-108.

Henry, P., Grall, C., Kende, J., Viseur, S., Özeren, M. S., Şengör, A. M. C., ... & Géli, L. (2018). A statistical approach to relationships between fluid emissions and faults: The Sea of Marmara case. Deep Sea Research Part II: *Topical Studies in Oceanography, 153,* 131-143.

Engels, J., & Grafarend, E. (1995). The oblique Mercator projection of the ellipsoid of revolution IE a 2, b. *Journal of Geodesy, 70(1-2*), 38-50.

Ergintav, S., McClusky, S., Hearn, E., Reilinger, R., Cakmak, R., Herring, T., ... & Tari, E. (2009). Seven years of postseismic deformation following the 1999, M= 7.4 and M= 7.2, Izmit-Düzce, Turkey earthquake sequence. *Journal of Geophysical Research: Solid Earth, 114*(B7).

Ergintav, S., R. E. Reilinger, R. Çakmak, M. Floyd, Z. Cakir, U. Doğan, R. W. King, S. McClusky, and H. Özener (2014). Istanbul's earthquake hot spots: Geodetic constraints on strain accumulation along faults in the Marmara seismic gap, *Geophys. Res. Lett., 41*, 5783–5788, doi:10.1002/2014GL060985.

Flerit, F., Armijo, R., King, G. C. P., Meyer, B., & Barka, A. (2003). Slip partitioning in the Sea of Marmara pull-apart determined from GPS velocity vectors. *Geophysical Journal International, 154(1),* 1-7.

Funiciello, F., Moroni, M., Piromallo, C., Faccenna, C., Cenedese, A., & Bui, H. A. (2006). Mapping mantle flow during retreating subduction: Laboratory models analyzed by feature tracking. *Journal of Geophysical Research: Solid Earth, 111*(B3),doi:10.1029/2005JB003792

Gasperini, L., Polonia, A., Çağatay, M. N., Bortoluzzi, G., & Ferrante, V. (2011). Geological slip rates along the North Anatolian Fault in the Marmara region. *Tectonics, 30*(6).

Grall, C., Henry, P., Tezcan, D., Mercier de Lepinay, B., Bécel, A., Géli, L., & Harmegnies, F. (2012). Heat flow in the Sea of Marmara Central Basin: Possible implications for the tectonic evolution of the North Anatolian fault. *Geology, 40(1*), 3-6.

Grall, C., Henry, P., Thomas, Y., Westbrook, G.K., Çağatay, M.N., Marsset, B., Saritas, H., Çifçi, G., Géli, L., (2013). Slip rate estimation along the western segment of the Main Marmara Fault over the last 405–490 ka by correlating mass transport deposits. *Tectonics 32,* 1–15.

Grall, C., Henry, P., Dupré, S., Geli, L., Scalabrin, C., Zitter, T. A., ... & Cifci, G. (2018). Upward migration of gas in an active tectonic basin: An example from the sea of Marmara. *Deep Sea Research Part II: Topical Studies in Oceanography, 153*, 17-35.

Graveleau, F., Malavieille, J., & Dominguez, S. (2012). Experimental modelling of orogenic wedges: A review. *Tectonophysics, 538*, 1-66.

Hergert, T., & Heidbach, O. (2011). Geomechanical model of the Marmara Sea region—II. 3-D contemporary background stress field. *Geophysical Journal International, 185*(3), 1090-1102.

Herece, E., and E. Akay (2003), Kuzey Anadolu Fayı (KAF) Atlası / Atlas of North Anatolian Fault (NAF), Maden Tetk. Arama Genel. Müdürlügü, Özel Yayın. Ser. 2 / General Directorate of Mineral Research and Exploration, Special Publications Series 2, Ankara, 61 pp. + 13 appendices as separate maps.

Hubert-Ferrari, A., Armijo, R., King, G., Meyer, B., & Barka, A. (2002). Morphology, displacement, and slip rates along the North Anatolian Fault, Turkey. *Journal of Geophysical Research: Solid Earth, 107*(B10), ETG-9.

Hussain, E., Wright, T. J., Walters, R. J., Bekaert, D., Hooper, A., & Houseman, G. A. (2016). Geodetic observations of postseismic creep in the decade after the 1999 Izmit earthquake, Turkey: Implications for a shallow slip deficit. *Journal of Geophysical Research: Solid Earth, 121(4),* 2980-3001.

Imren, C., Le Pichon, X., Rangin, C., Demirbağ, E., Ecevitoğlu, B., & Görür, N. (2001). The North Anatolian Fault within the Sea of Marmara: a new interpretation based on multi-channel seismic and multi-beam bathymetry data. *Earth and Planetary Science Letters, 186(2),* 143-158.

Kende, J., Henry, P., Bayrakci, G., Özeren, M. S., & Grall, C. (2017). Moho depth and crustal thinning in the Marmara Sea region from gravity data inversion. *Journal of Geophysical Research: Solid Earth, 122(2),* 1381-1401.

Klinkmüller, M., Schreurs, G., Rosenau, M., & Kemnitz, H. (2016). Properties of granular analogue model materials: A community wide survey. *Tectonophysics, 684*, 23-38.

Koçyiğit, A. (1988). Tectonic setting of the Geyve Basin: Age and total displacement of the Geyve Fault Zone. *METU Journal of Pure and Applied Sciences, 21*, 81-104.

Kozacı, Ö., Dolan, J. F., & Finkel, R. C. (2009). A late Holocene slip rate for the central North Anatolian fault, at Tahtaköprü, Turkey, from cosmogenic 10Be geochronology: Implications for fault loading and strain release rates. *Journal of Geophysical Research: Solid Earth, 114*(B1).

Kurt, H., et al. (2013), Steady late quaternary slip rate on the Cinarcik section of the North Anatolian fault near Istanbul, Turkey, *Geophys. Res. Lett., 40,* 4555–4559, doi:10.1002/grl.50882.

Laigle, M., Becel, A., de Voogd, B., Hirn, A., Taymaz, T., & Ozalaybey, S. (2008). A first deep seismic survey in the Sea of Marmara: Deep basins and whole crust architecture and evolution. *Earth and Planetary Science Letters, 270*(3-4), 168-179.

Le Pichon, X., Şengör, A. M. C., Demirbağ, E., Rangin, C., Imren, C., Armijo, R., ... & Saatçılar, R. (2001). *The active main Marmara fault. Earth and Planetary Science Letters, 192(4),* 595-616

Le Pichon, X., N. Rangin, C. Chamot-Rooke, and A. M. C. Sengör, 2003. The North Anatolian Fault in the Sea of Marmara, *J. Geophys. Res., 108(B4),* 2179.

Le Pichon, X., Imren, C., Rangin, C., Şengör, A. C., & Siyako, M. (2014). The South Marmara Fault. *International Journal of Earth Sciences, 103(1),* 219-231.

Mann, P. (2007). Global catalogue, classification and tectonic origins of restraining-and releasing bends on active and ancient strike-slip fault systems. *Geological Society, London, Special Publications, 290*(1), 13-142.

Meghraoui, M., & Pondrelli, S. (2013). Active faulting and transpression tectonics along the plate boundary in North Africa. *Annals of Geophysics, 55*(5).

Nestola, Y., Storti, F., Bedogni, E., & Cavozzi, C. (2013). Shape evolution and finite deformation pattern in analog experiments of lithosphere necking. *Geophysical Research Letters, 40*(19), 5052-5057.

McClay, K., & Dooley, T. (1995). Analogue models of pull-apart basins. *Geology, 23*(8), 711-714.

McClay, K. R., & White, M. J. (1995). Analogue modelling of orthogonal and oblique rifting. Marine and Petroleum *Geology, 12*(2), 137-151.

McClay, K., & Bonora, M. (2001). Analog models of restraining stepovers in strike-slip fault systems. *AAPG bulletin, 85*(2), 233-260.

Muller, J. R., & Aydin, A. (2005). Using mechanical modeling to constrain fault geometries proposed for the northern Marmara Sea. *Journal of Geophysical Research: Solid Earth, 110*(B3).

Okay, A. I., Demirbağ, E., Kurt, H., Okay, N., & Kuşçu, İ. (1999). An active, deep marine strike-slip basin along the North Anatolian fault in Turkey. *Tectonics, 18*(1), 129-147.

Okay, A. I., A. Kaslilar-Ozcan, C. Imren, A. Boztepe-Guney, E. Demirbag, and I. Kuscu (2000), Active faults and evolving strike-slip basins in the Marmara Sea, Northwest Turkey: A multichannel seismic reflection study, *Tectonophysics*, ***321***, 189–218.

Okay, A. I., Tüysüz, O., & Kaya, Ş. (2004). From transpression to transtension: changes in morphology and structure around a bend on the North Anatolian Fault in the Marmara region. *Tectonophysics, 391*(1-4), 259-282.

Özalp, S., Emre, Ö., & Doğan, A. (2013). The segment structure of southern branch of the North Anatolian Fault and paleoseismological behaviour of the Gemlik Fault, NW Anatolia. *General Directorate of Mineral Research and Exploration (MTA) Bulletin, 147*, 1-17.

Rahe, B., Ferrill, D. A., & Morris, A. P. (1998). Physical analog modeling of pull-apart basin evolution. *Tectonophysics, 285*(1-2), 21-40.

Reilinger, R., & McClusky, S. (2011). Nubia–Arabia–Eurasia plate motions and the dynamics of Mediterranean and Middle East tectonics. *Geophysical Journal International, 186*(3), 971-979.

Reilinger, R., McClusky, S., Vernant, P., Lawrence, S., Ergintav, S., Cakmak, R., ... & Nadariya, M. (2006). GPS constraints on continental deformation in the Africa-Arabia-Eurasia continental collision zone and implications for the dynamics of plate interactions. *Journal of Geophysical Research: Solid Earth, 111*(B5).

Schreurs, G., Hänni, R., Panien, M., & Vock, P. (2003). Analysis of analogue models by helical X-ray computed tomography. *Geological Society, London, Special Publications, 215*(1), 213-223.

Schreurs, G., Buiter, S. J., Boutelier, D., Corti, G., Costa, E., Cruden, A. R., ... & Lohrmann, J. (2006). Analogue benchmarks of shortening and extension experiments. *Special Publication-Geological Society of London, 253*, 1.

Schreurs, G., Buiter, S. J., Boutelier, J., Burberry, C., Callot, J. P., Cavozzi, C., ... & Cruz, L. (2016). Benchmarking analogue models of brittle thrust wedges. *Journal of structural geology*, 92, 116-139.

Seeber, L., O. Emre, M.-H. Cormier, C. C. Sorlien, C. M. G. McHugh, A. Polonia, N. Ozer, and N. Cagatay (2004), Uplift and subsidence from oblique slip: The Ganos-Marmara bend and the North Anatolian Transform, western Turkey, *Tectonophysics, 391*, 239–258.

Seeber, L., Cormier, M. H., McHugh, C., Emre, O., Polonia, A., & Sorlien, C. (2006). Rapid subsidence and sedimentation from oblique slip near a bend on the North Anatolian transform fault in the Marmara Sea, Turkey. *Geology, 34*(11), 933-936.

Seeber, L., Sorlien, C., Steckler, M., & Cormier, M. H. (2010). Continental transform basins: Why are they asymmetric?. *Eos, Transactions American Geophysical Union, 91*(4), 29-30.

Sims, D., Ferrill, D. A., & Stamatakos, J. A. (1999). Role of a ductile decollement in the development of pull-apart basins: Experimental results and natural examples. *Journal of Structural Geology, 21*(5), 533-554.

Sorlien, C. C., Akhun, S. D., Seeber, L., Steckler, M. S., Shillington, D. J., Kurt, H., ... & İmren, C. (2012). Uniform basin growth over the last 500 ka, North Anatolian Fault, Marmara Sea, Turkey. *Tectonophysics, 518*, 1-16.

Sugan, M., Wu, J. E. L., & McClay, K. (2014). 3D analogue modelling of transtensional pull-apart basins: comparison with the Cinarcik basin, Sea of Marmara, Turkey. *Bollettino di Geofisica Teorica ed Applicata, 55*(4).

Şengör, A. M. C., Tüysüz, O., Imren, C., Sakınç, M., Eyidoğan, H., Görür, N., & Rangin, C. (2005). The North Anatolian fault: A new look. *Annu. Rev. Earth Planet. Sci., 33*, 37-112.

Şengör, A. C., Grall, C., İmren, C., Le Pichon, X., Görür, N., Henry, P., ... & Siyako, M. (2014). The geometry of the North Anatolian transform fault in the Sea of Marmara and its temporal evolution: implications for the development of intracontinental transform faults. *Canadian Journal of Earth Sciences*, *51*(3), 222-242.

Thielicke, W and Stamhuis, E J 2014 PIVlab – Towards User-friendly, A ordable and Accurate Digital Particle Image Velocimetry in MATLAB. *Journal of Open Research Software*, *2*: e30, DOI: http://dx.doi.org/10.5334/jors.bl

Toeneboehn, K. (2017). Exploring Long-term Fault Evolution in Obliquely Loaded Systems Using Tabletop Experiments and Digital Image Correlation Techniques.

Yaltırak, C. (2002). Tectonic evolution of the Marmara Sea and its surroundings. *Marine Geology, 190*(1-2), 493-529.

White, D. J., Take, W. A., & Bolton, M. D. (2001, September). Measuring soil deformation in geotechnical models using digital images and PIV analysis. In 10th international conference on computer methods and advances in geomechanics (No. 1, pp. 997-1002).

Wolf, H., König, D., & Triantafyllidis, T. (2003). Experimental investigation of shear band patterns in granular material. *Journal of Structural Geology, 25*(8), 1229-1240.

Wu, J. E., McClay, K., Whitehouse, P., & Dooley, T. (2009). 4D analogue modelling of transtensional pull-apart basins. *Marine and Petroleum Geology, 26*(8), 1608-1623.

853 **Table 1 Mechanical and physical properties of the materials used in the model**

Materials	Density (g/cm^3)	Mean grain size (μm)	Peak Cohesion (Pa)	Angle of internal friction φ	Dynamic shear viscosity η (Pa s)
Sand[1]	1.670	224	102	33°	- - - -
Silicone + barite[2]	1.150	- - - -	- - - -	- - - -	$1{,}4 \times 10^4$

854 [1] Upper crust (from Klinkmüller et al., 2016)
855 [2] Weak lower crust (from Cappelletti et al., 2013)
856
857
858
859
860
861
862
863
864
865
866
867
868
869
870
871
872
873
874
875
876
877
878
879
880

Figure 1. Tectonic map of the North Anatolian Fault in the Sea of Marmara region (simplified from Grall et al., 2013 et al., Gasperini et al., 2011). The inset shows the tectonic setting of the Anatolian plate. Plate motions are with respect to the Eurasian plate. KTJ is the Karliova triple Junction. EAF is the East Anatolian Fault.This natural system motivates the geometry chosen for the analogue experiments in this study. NAF Northern strand represents the NAF-N in the text. NAF Southern strand represents the NAF-S in the text.

Figure 2. Simplified, tectonic models proposed for the tectonic evolution of the Sea of Marmara. a) the pull-apart model (Armijo, et al., 1999, 2002), b) the en-echelon fault segment model (Okay et al., 2000, 2004. c) the single thoroughgoing fault (LePichon et al., 2001, 2003; Seeber et al., 2004).

Figure 3. a) Simplified fault map trace used to produce the Plexiglas basal plate. Bathymetric metadata and Digital Terrain Model data products are derived from the EMODnet Bathymetry portal - http://www.emodnet-bathymetry.eu. (b) Setup of sand box experiments, initial pre-cut fault setup with its analogue scaled lengths in 3d perspective. Model scale is 1cm per 10 km. The moving plate was placed on a fixed basal plate.

Figure 4. *Undeformed experimental stratigraphy of the experiments. Dashed line represents the anticipated basin subsidence after deformation of the model.*

Fig. 5. Overhead photographs illustrating the evolution of the experiment at 10 mm displacement steps. See text for details. + indicates the region north of the NAF, which is fixed in the experiment. The white arrow shows the direction of translation of the mobile Plexiglas basal plate. The ruler on the right-bottom represents the 5 cm displacement on the basal plate that was applied over each entire experiment.

Figure 6 shows the vorticity patterns and velocity vectors during each 5mm step of displacement. A colorblind-friendly version of this image is available in the Supporting Information (S_1).

Figure 7. Comparison the shear rate, topographic changes, and areal strain at prominent times, between 15 mm-20 mm(a,b,c) , 25 mm -30 mm(d,e,f) and 45 mm-50 mm(g,h,i) of displacement. The unit ot he shear rate is 1/m, the unit of areal strain is dimensionless (m/m). See text for details. Colour-blind friendly version is available in the Supporting Information (S_2).

Figure 8. Model topography changes superimposed onto the map of the Sea of Marmara, including the traces of major fault zones pertaining to the northern North Anatolian Fault. The projection system was converted from WGS 84 to Oblique Mercator in order to correct for the flat model of the Sea of Marmara fault system. White arrows represent the direction of motion of the base of the analogue model; the black cross is on the fixed plate. A colorblind-friendly version of this image is available in the Supporting Information (S_3).

Figure 1.

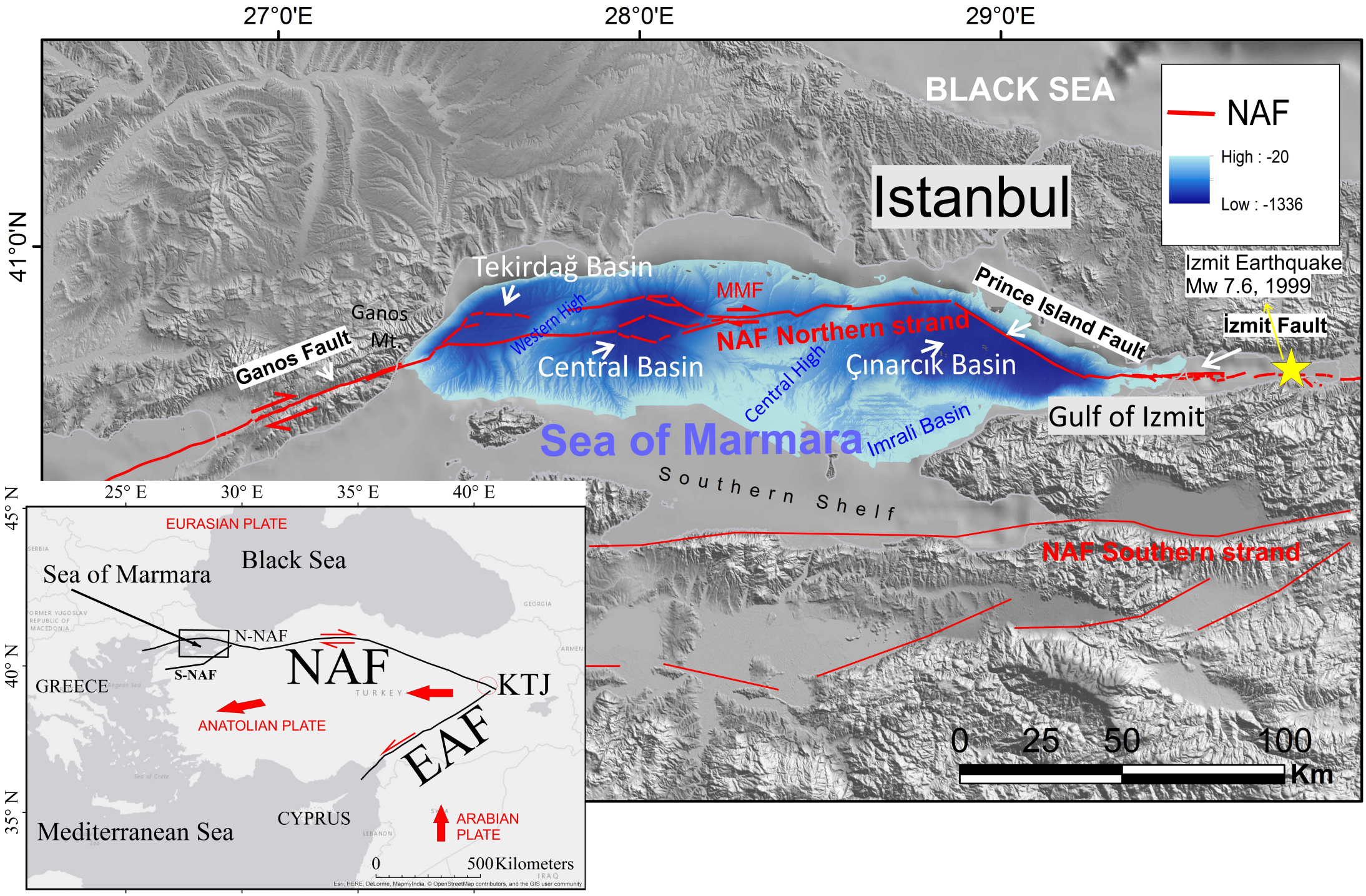
27°0'E
28°0'E
29°0'E
41°0'N
BLACK SEA
NAF
High : -20
Low : -1336
Istanbul
Izmit Earthquake
Mw 7.6, 1999
İzmit Fault
Tekirdağ Basin
MMF
Western High
Prince Island Fault
Ganos Mt.
Ganos Fault
NAF Northern strand
Central Basin
Central High
Çınarcık Basin
Gulf of Izmit
Sea of Marmara
Imrali Basin
Southern Shelf
NAF Southern strand
0 25 50 100
Km
25° E
30° E
35° E
40° E
45° N
40° N
35° N
EURASIAN PLATE
Sea of Marmara
Black Sea
N-NAF
S-NAF
NAF
KTJ
GREECE
TURKEY
ANATOLIAN PLATE
EAF
CYPRUS
ARABIAN PLATE
Mediterranean Sea
0 500 Kilometers
Esri, HERE, DeLorme, MapmyIndia, © OpenStreetMap contributors, and the GIS user community

Figure 2.

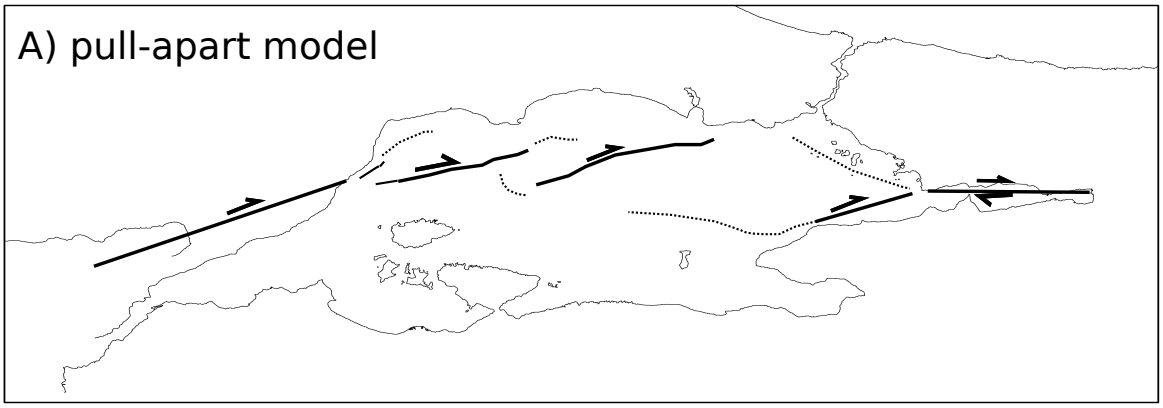
A) pull-apart model

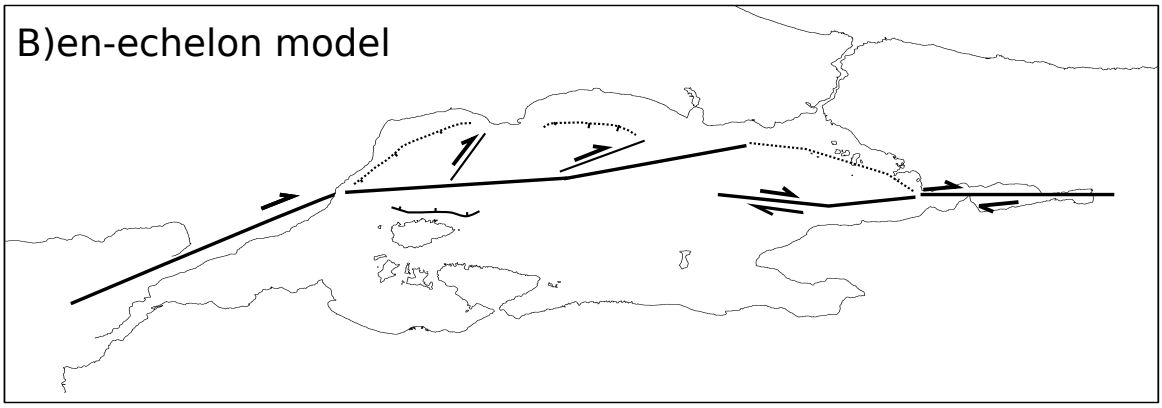
B)en-echelon model

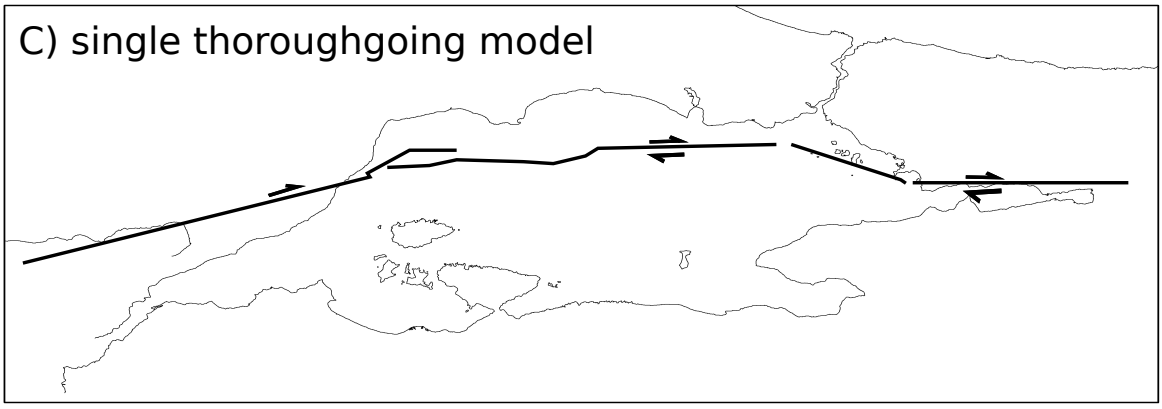
C) single thoroughgoing model

Figure 3.

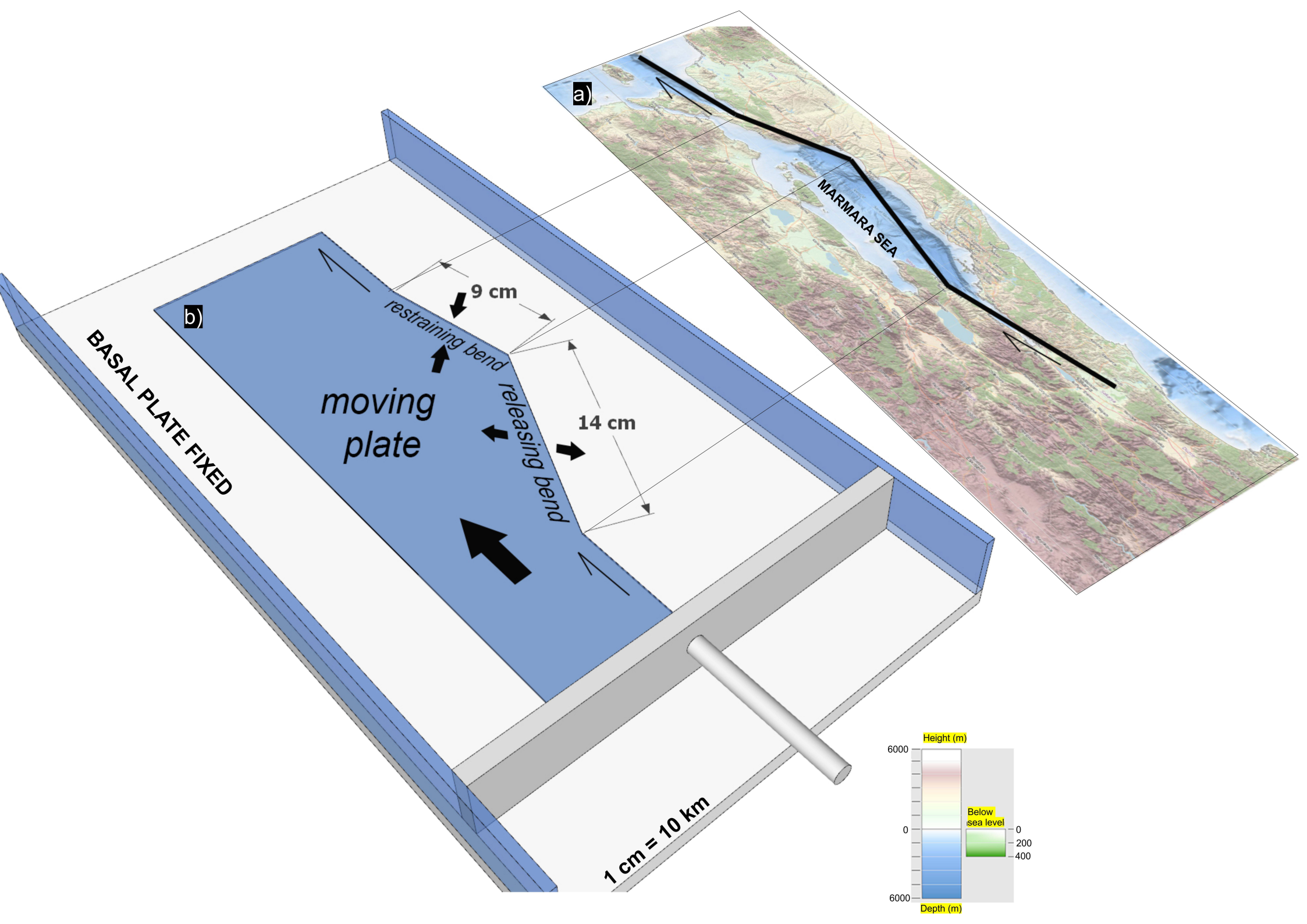
a)
MARMARA SEA
b)
9 cm
restraining bend
releasing bend
moving plate
14 cm
BASAL PLATE FIXED
1 cm = 10 km
Height (m)
6000
0
6000
Depth (m)
Below sea level
0
200
400

Figure 4.

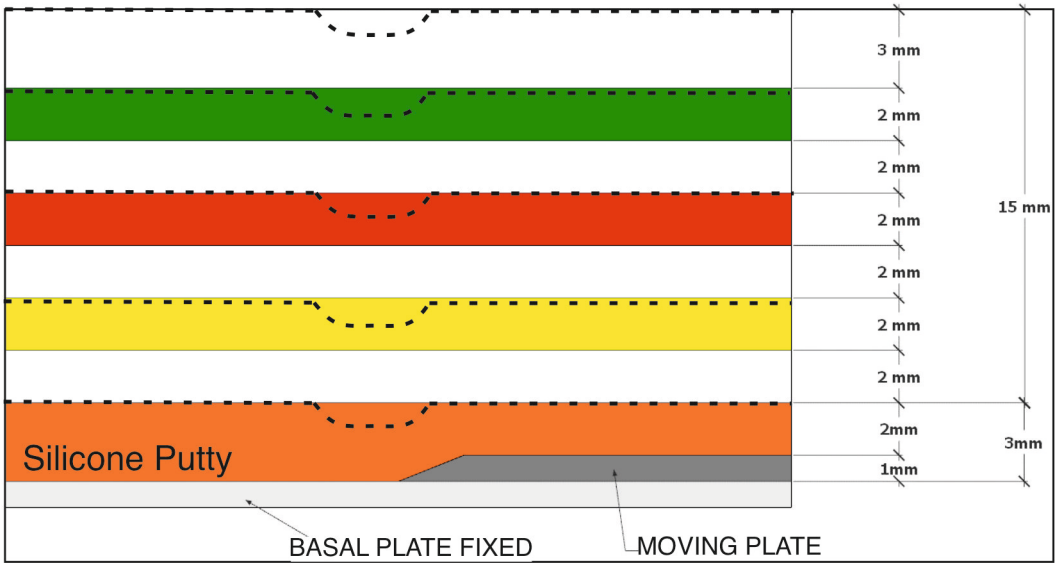
3 mm
2 mm
2 mm
2 mm
2 mm
2 mm
2 mm
2mm
1mm
15 mm
3mm
Silicone Putty
BASAL PLATE FIXED
MOVING PLATE

Figure 5.

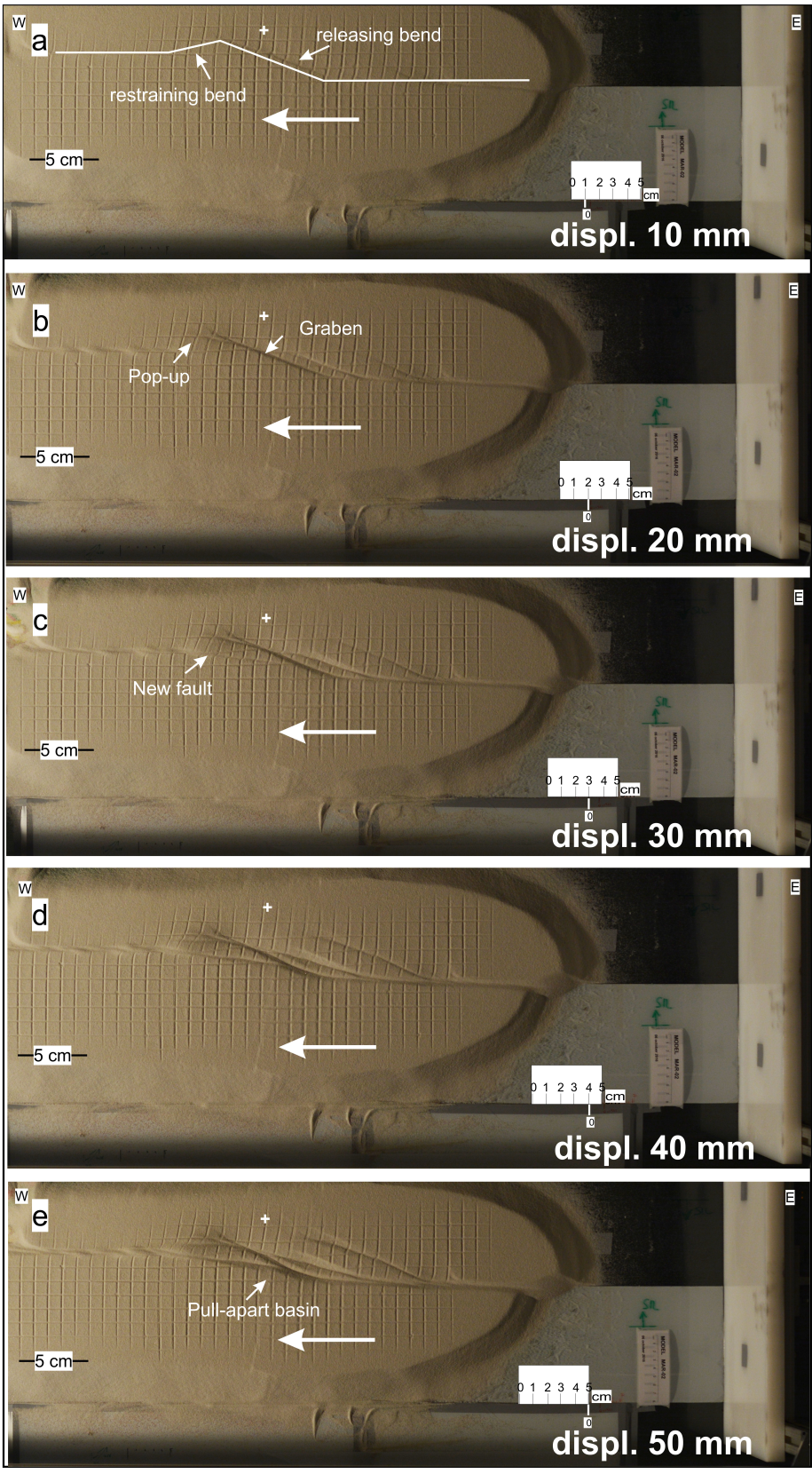
W
E
a
releasing bend
restraining bend
5 cm
displ. 10 mm
b
Graben
Pop-up
displ. 20 mm
c
New fault
displ. 30 mm
d
displ. 40 mm
e
Pull-apart basin
displ. 50 mm

Figure 6.

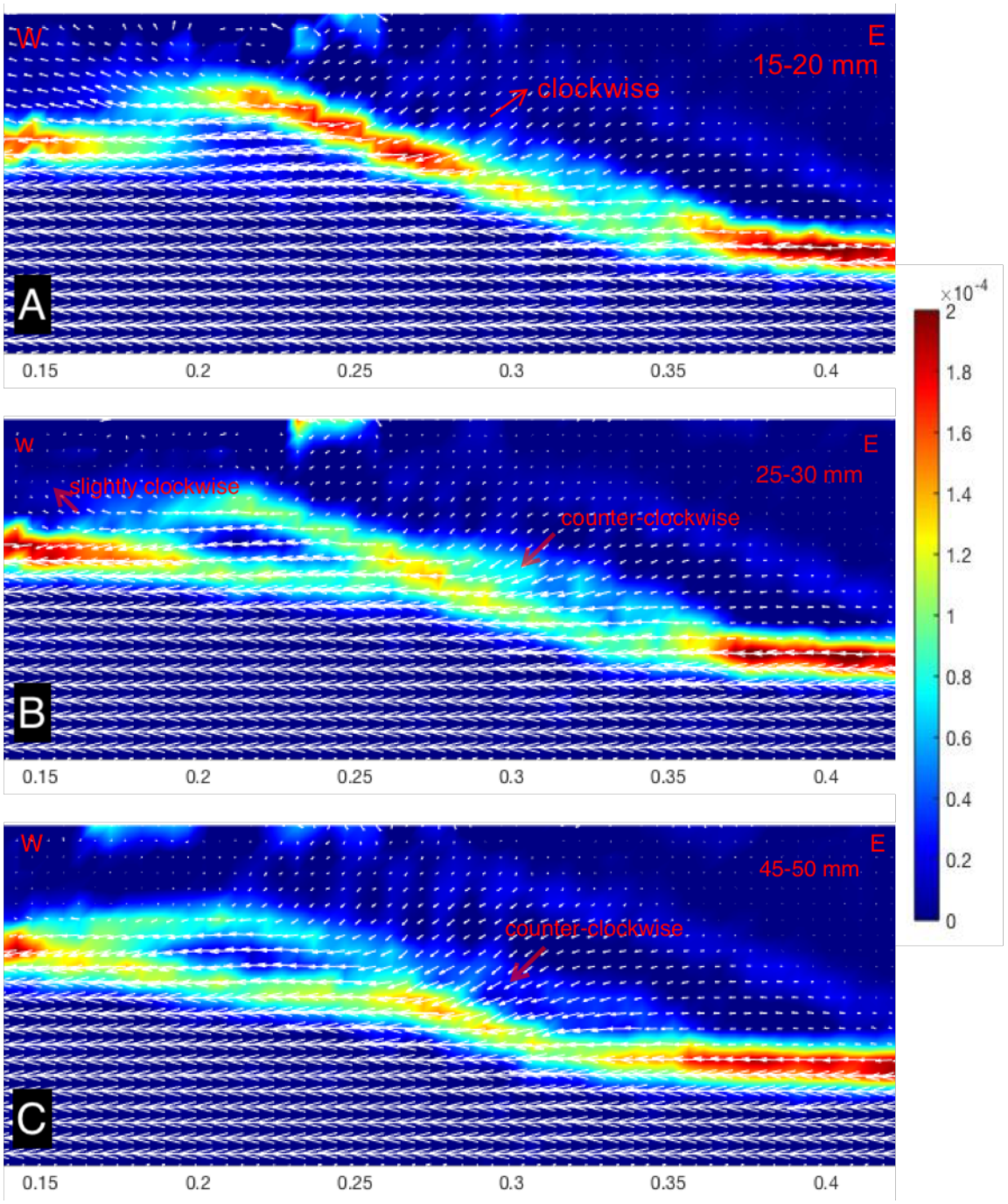
W
E
15-20 mm
clockwise
A
0.15
0.2
0.25
0.3
0.35
0.4
W
E
25-30 mm
slightly clockwise
counter-clockwise
B
0.15
0.2
0.25
0.3
0.35
0.4
W
E
45-50 mm
counter-clockwise
C
0.15
0.2
0.25
0.3
0.35
0.4
×10^-4
2
1.8
1.6
1.4
1.2
1
0.8
0.6
0.4
0.2
0
Angular Velocity 1/s

Figure 7.

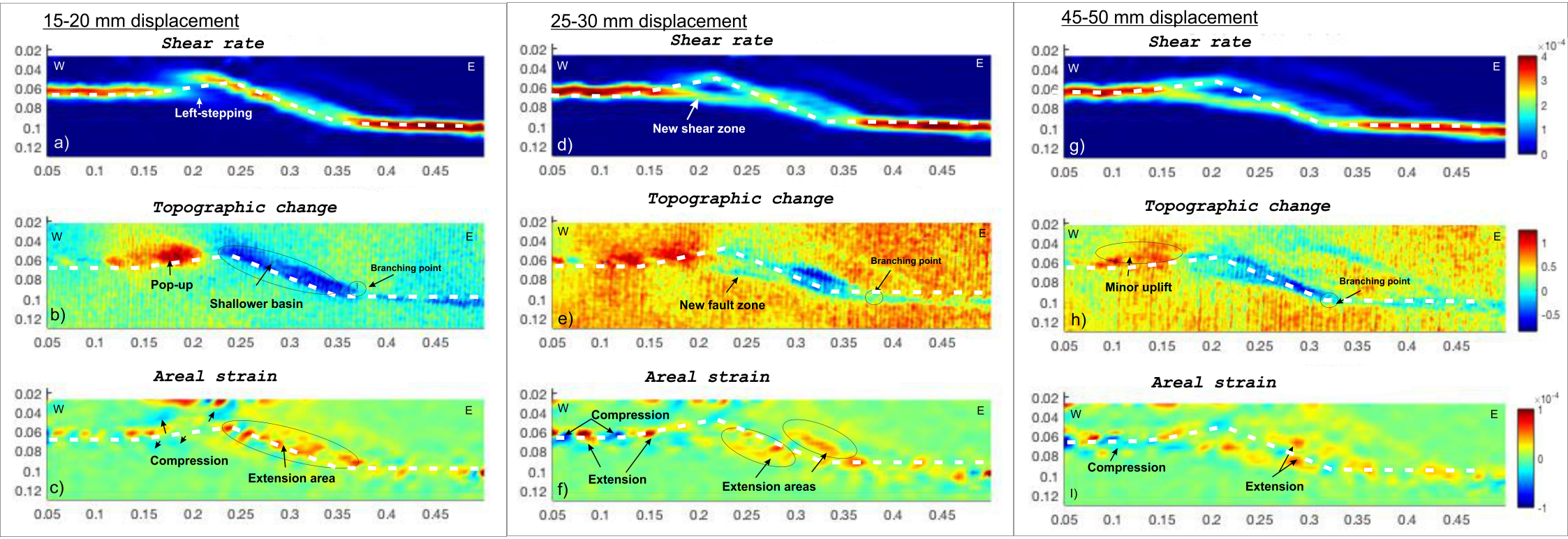
15-20 mm displacement
Shear rate
W
E
Left-stepping
a)
Topographic change
Pop-up
Shallower basin
Branching point
b)
Areal strain
Compression
Extension area
c)
25-30 mm displacement
Shear rate
New shear zone
d)
Topographic change
New fault zone
Branching point
e)
Areal strain
Compression
Extension
Extension areas
f)
45-50 mm displacement
Shear rate
g)
Topographic change
Minor uplift
Branching point
h)
Areal strain
Compression
Extension
I)
0.05 0.1 0.15 0.2 0.25 0.3 0.35 0.4 0.45
0.02 0.04 0.06 0.08 0.1 0.12

Figure 8.

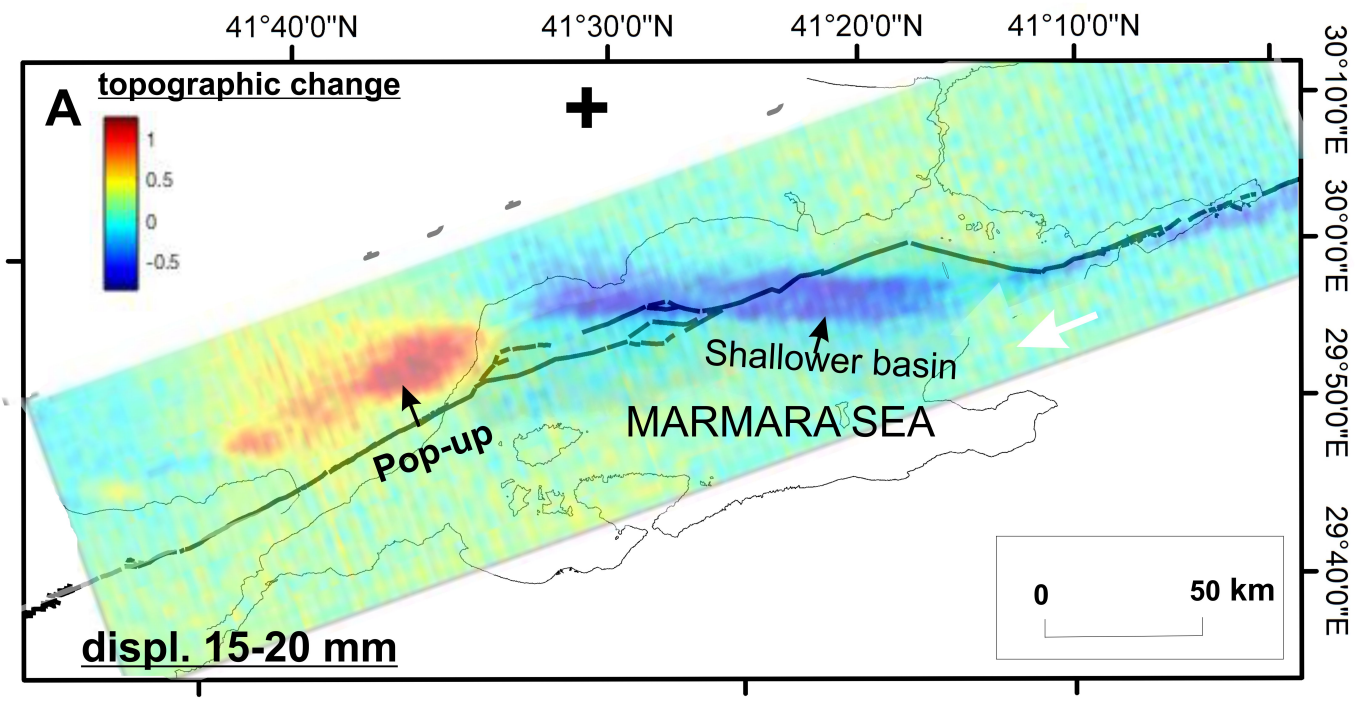
41°40'0"N
41°30'0"N
41°20'0"N
41°10'0"N
30°10'0"E
30°0'0"E
29°50'0"E
29°40'0"E
A
topographic change
1
0.5
0
-0.5
Shallower basin
Pop-up
MARMARA SEA
0
50 km
displ. 15-20 mm

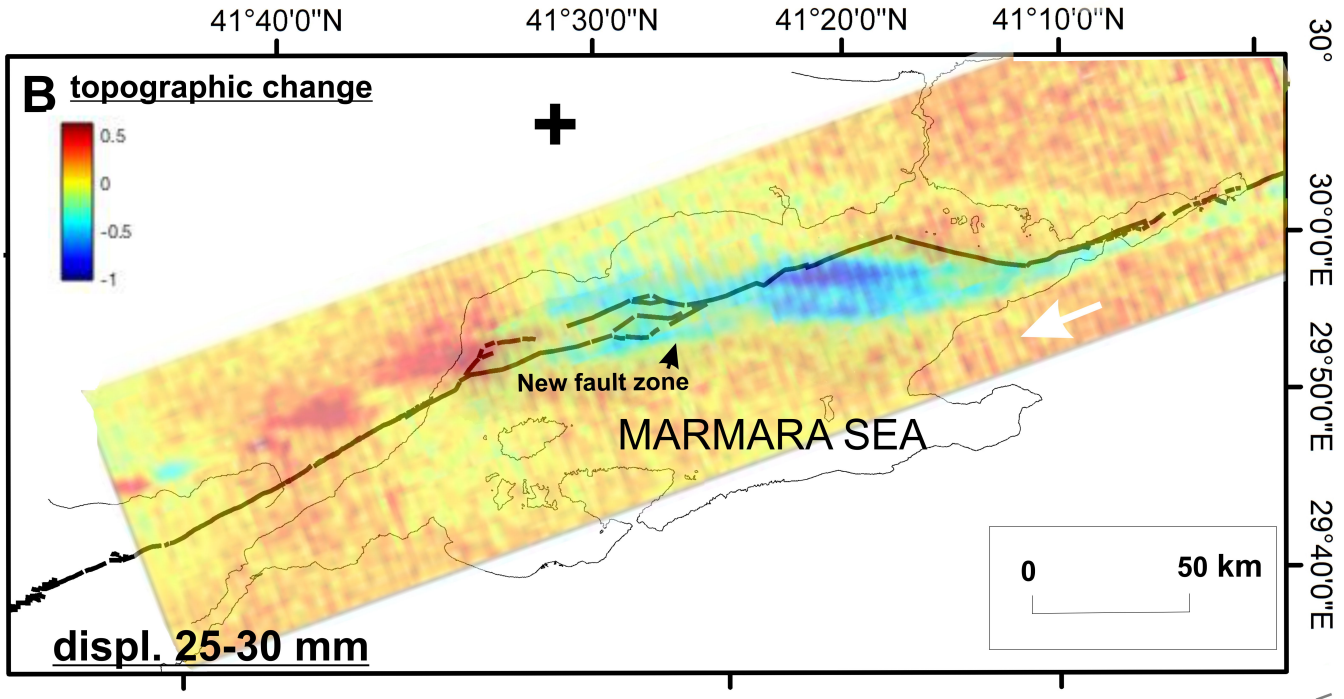
41°40'0"N
41°30'0"N
41°20'0"N
41°10'0"N
30°
30°0'0"E
29°50'0"E
29°40'0"E
B
topographic change
0.5
0
-0.5
-1
New fault zone
MARMARA SEA
0
50 km
displ. 25-30 mm

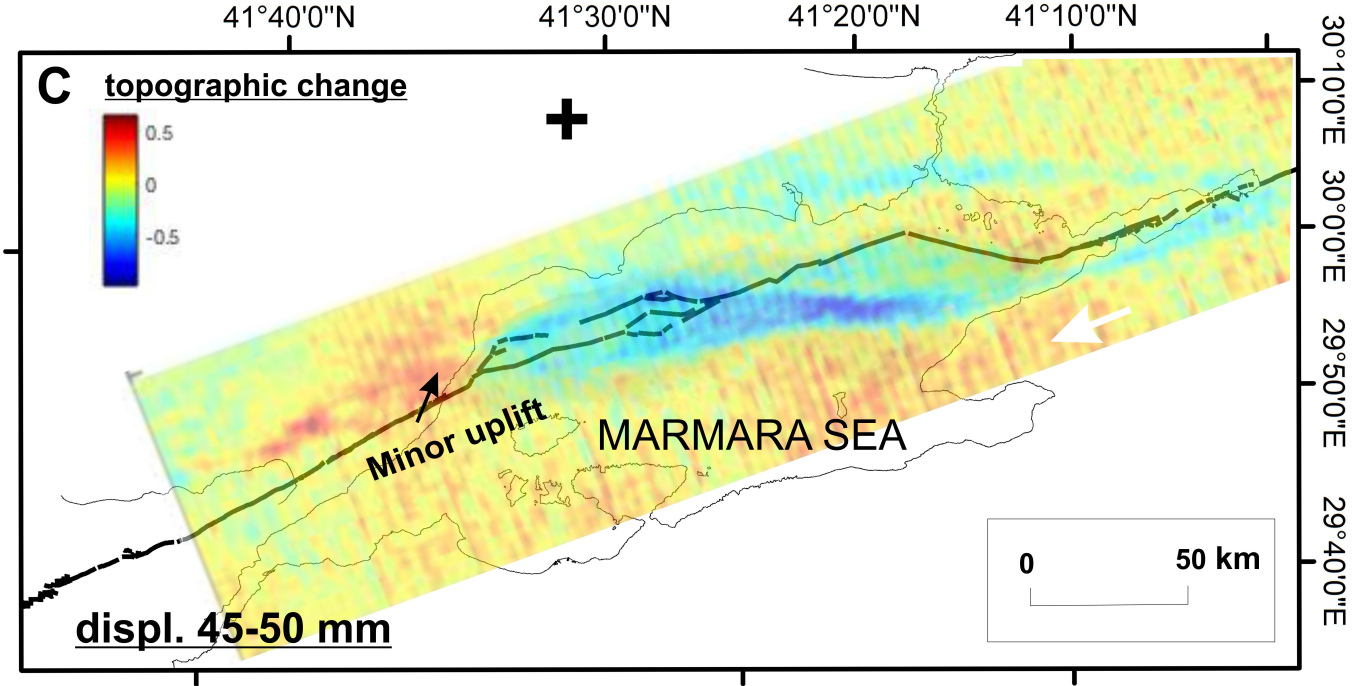
41°40'0"N
41°30'0"N
41°20'0"N
41°10'0"N
30°10'0"E
30°0'0"E
29°50'0"E
29°40'0"E
C
topographic change
0.5
0
-0.5
Minor uplift
MARMARA SEA
0
50 km
displ. 45-50 mm